Hindawi
Science and Technology of Nuclear Installations
Volume 2022, Article ID 3676334, 13 pages
https://doi.org/10.1155/2022/3676334

Research Article

Investigation of Oxidation and Counter-Oxidation in a One-Quarter Circular Geometry due to Shadow Corrosion

Doctor Enivweru,[1,2] **Qingyu Wang**,[1] **Abiodun Ayodeji**,[2,3] **and Yu Zhou**[1]

[1]*College of Nuclear Science and Technology, Harbin Engineering University, No. 145 Nantong Street, Nangang District, Harbin 150001, China*
[2]*Nigeria Atomic Energy Commission, 9 Kwame Nkrumah Crescent, Asokoro, P.M.B. 646 Garki, Abuja, Nigeria*
[3]*State Key Laboratory of Industrial Control Technology, College of Control Science and Engineering, Zhejiang University, Hangzhou 310027, China*

Correspondence should be addressed to Qingyu Wang; wangqingyu@hrbeu.edu.cn

Received 30 April 2022; Revised 15 June 2022; Accepted 4 July 2022; Published 9 August 2022

Academic Editor: Raffaella Testoni

To optimize fission fuel and protect cladding integrity, this work investigates shadow corrosion in a one-fourth circular electrode geometry. The anodic corrosion of Zircaloy-2 (Zry-2) was investigated in a circular geometry electrode configuration under reactor operating conditions. The impact of gamma and neutron radiations on water conductivity and shadow corrosion was examined under two different cathodes. This work also investigates the effect of current exchange density and the cathodic Tafel coefficient on the cathodic current. Using COMSOL Multiphysics 5.2, the Laplace equation was solved to obtain the electrostatic potential and current density distributions in the studied domain. When the distance d between the anode (Zry-2) and cathode (platinum/nickel) is ≤0.5 mm, it was observed that a uniform oxide layer of thickness 20 μm grew on the smooth internal surface of Zry-2 for corrosion lasting 1166 h. When $d > 0.5$ mm, the oxide thickness falls in a manner dictated by the degree of dissociation α of the electrolyte. At a cladding gap of 0.08 mm, a radiation-enhanced uniform corrosion rate of $2.405\,10^{-1}$ mmpy was obtained for Zry-2. This value is 142 times greater than that obtained at room temperature in the absence of radiation. It was also observed that the corrosion rate falls at higher cladding gaps, and the rate of change depends on the degree of dissociation. Other phenomena such as the dynamics of shadow corrosion under varying electrode separation and electrolyte conductivities, as well as extensive evaluation of critical fuel cladding parameters, are presented in this work.

1. Introduction

Due to the increase in energy consumption, the task of optimization of fission fuels, and the cumbersome nature of producing new kinds of reactors, the longevity and integrity of fuel cladding have become essential. The long-lifetime achievement of this core component is retarded under irradiation conditions. This is a result of corrosion/oxidation degradation of structural materials when exposed to ionizing radiations [1]. In general, unless electrons are transferred from the metal to water and oxygen ions diffuse in the opposite direction of electrons, the corrosion or oxidation reaction in Zircaloys is unlikely to happen [1]. As a result, oxygen ion diffusion and electron mobility are critical in oxidation, with the slower traveling species acting as the rate-controlling process. Several investigations with and without irradiation have been conducted to better understand the oxidation mechanism of Zircaloys. Placing the specimens in molten salt, for example, revealed the complex behavior of current in Zircaloy-2 oxides, with the electronic and ionic currents following the Schottky emission and Tafel relationships, respectively [2]. Both electrons and ions were shown to be equally significant in the rate-controlling process [3]. Shirvington discovered electron conduction that is unaffected by oxidation environments in two types of Zircaloy-2 oxides formed in oxygenated water under the fast neutron flux of 1.5×10^{13} n/cm^2 s with fluoride contamination (in reactor oxide) and in the steam of a micro-

autoclave (out reactor oxide) [2]. The effect of 29.2 Gy/s gamma irradiation on electron transport in Zircaloy-2 oxides was also discovered [4].

Shadow corrosion is a phrase used in the nuclear industry to indicate increased corrosion of Zircaloys in a boiling water reactor (BWR) when it is near or in contact with another metallic component that is usually nobler than the Zircaloy [5]. The localized accelerated corrosion resembles the form of the other noble component, which resembles a shadow [5]. Due to the potential difference between Zircaloys and the other metal component under radiolysis in a BWR-type environment, shadow corrosion (SC) has been hypothesized to be a particular example of crevice corrosion. When SC is detected, however, the separation between Zircaloys and the dissimilar metal component is not a crevice. The effect of SC, for example, can be visible at gaps ranging from a fraction of a millimeter to a few millimeters, whereas typical crevices are only a few tens of nanometers wide. The electrochemical basis for the accelerated corrosion is strongly suggested by the observed potentials and short circuit currents, implying that galvanic corrosion could be the cause. However, there is no direct electrical contact between Zircaloy-2 and the other material producing the shadow effect. Although the photoconductivity of the oxides and greater coolant conductivity have been suggested as variables in the current flow between the two metals, the specific mechanism for the enhanced corrosion is yet unknown [3]. In his conclusion, Ramasubramanian [3] stated that when Zircaloy-2 is near platinum or nickel alloys under BWR conditions: (1) Shadow corrosion is initiated by proton transport to Zircaloy-2, which is aided by the potential difference between the two materials; (2) coupling of the two materials is via ionic transport in the coolant in the gap, which is aided by the potential difference between the two metals, and the transport of species under their concentration gradients; and (3) radiolysis is required for the hypothesized electrochemical mechanism to function, as it ensures that a minimum concentration of radiolytic species is present.

SC has been adjudged as a phenomenon peculiar only to BWRs [6], and the results of experiments at the Massachusetts Institute of Technology (MIT) support the galvanic coupling paradigm as the cause of SC [7]. SC develops only when a counter-electrode (CE) consisting of a nobler metal than the Zircaloy is used, and the thickness of the oxide layer formed decreases as the distance between electrodes rises. While aluminium oxide successfully separates the cladding from the CE, this layer cannot be termed insulating because it is thin (a few millimeters) and its electrical conductivity increases when exposed to light due to a photoconductivity effect [8, 9]. The MIT experiments have been used as a reference standard of validation for studies involving SC in commercial reactors [7]. The experiments revealed that with a 0.5 mm gap between Zircaloy-2 (anode) and platinum (cathode), an oxide layer of 20 μm was developed on the surface of Zircaloy-2 for corrosion lasting 1166 hours. Factors impacting shadow corrosion in a BWR environment with platinum as the CE were explored using the MIT standard in a modeling study of the galvanic coupling process in a BWR environment [7]. It was shown that regardless of the nature of the CE, the same oxide thickness could be achieved as long as it was made of a metal nobler than Zircaloys. More recently, the precise control of proton flux and estimated hydrogen peroxide concentration, as well as comprehensive oxide thickness measurements, were used to develop an empirical model for shadow corrosion under neutron irradiation [10]. These studies, however, are limited as they considered only the plane electrode geometry, which is rarely the case in the real world. Furthermore, previous studies failed to address the effect of ionizing radiations on the electrolyte conductivity.

To address the limitation with the state of the art, and to further optimize fission fuel, the current work investigates the effect of ionizing radiations on SC that may occur at the cladding gap of a cracked fuel pellet in a BWR, where platinum/nickel alloys are used as a surrogate fuel (the cathode). The crack creates an avenue for water ingress into the cladding gap. In order to make the computational time smaller and to ensure an angle of 90° between two crack locations, a portion (one-quarter) of the actual circular domain is chosen for study in this work. First, to validate the model used in the current work, the MIT standard is implemented through SC simulation in a ¼ circular electrode geometry in other to establish the referenced oxide thickness. Second, using this as a benchmark, a new model is developed that considers the peculiarities of a cracked fuel pellet where the radiation field impacts the conductivity of the coolant water in the cladding gap. The distribution of electric potential and current in the investigated geometry is carried out using the electrochemistry module of COMSOL Multiphysics 5.2. This work advances the state of the art by (1) developing a new galvanic coupling model in a BWR environment with circular geometry and cracked pellet; (2) investigating the effect of ionizing radiations on the electrolyte conductivity and shadow corrosion under two different cathodes: platinum and Alloy 718 (referred to as the nickel alloy or nickel subsequently); (3) establishing the relationship between the cladding gap, the rate of change of corrosion, and the electrolyte degree of dissociation for different fuel geometries; and (4) presenting the differences between shadow corrosion in plane and one-fourth circular geometries.

Furthermore, this work also investigates the effect of the density of current exchange at the cathode and the cathodic Tafel coefficient on the cathodic current. The experiment was done by running two parallel simulations with two different cathodes (platinum and nickel) while keeping the anode (Zircaloy-2) constant, and the result is presented in this paper. This work is useful in understanding the similarities and differences between the shadow corrosion in one-fourth circular and plane geometries. Although the UO_2 fuel is a ceramic material, a parametric study was also carried out using the electrochemical properties of UO_2 fuel in order to obtain practical results in a BWR environment.

2. Materials and Methods

2.1. Model Geometry and Boundary Conditions. The system geometry adopted in this work is fashioned after Lysell's

electrochemical mechanism of SC where a platinum CE is electrically connected to a Zircaloy anode via an electrolyte [7] as depicted in Figure 1. The electrolyte occupies a distance d between the two opposing electrodes.

In the current study, the CE is chosen as platinum in the first scenario and Alloy 718 is taken as CE in the second scenario. The chemical compositions of Alloy 718 and Zircaloy-2 (Zry-2) are provided in Tables 1 and 2, respectively. Both electrodes are separated by a gap occupied by coolant water of variable width d.

The model considers ¼ of a fuel pellet where a 1° crack leads to the ingress of coolant water into the cladding gap. For simplicity, the effect of the crack beyond water ingress into the cladding gap is not considered in this study. The CE has a radius of 4 mm, and the anode has a thickness of 0.65 mm. The entire geometry subtends an angle of 90° at the center; hence, the lengths of the arcs (electrode surfaces) at the boundaries are known (Figure 2).

The model geometry used in this study is shown in Figure 2. A counter-electrode (platinum/nickel) is positioned opposite Zry-2 (the anode). Both electrodes are in electrical contact via irradiated water in the cladding gap with variable width d. Points on the inner surface of the clad (site of oxidation) are identified by the one-dimensional coordinate along the x-axis. The following assumptions are made for this simulation:

(i) The total area of the CE is less than that of the anode (geometry dimensions chosen to ensure this condition).

(ii) The CE is nobler than the anode (i.e., the anode corrodes preferentially to the cathode).

(iii) The thickness of the oxide layer at the initial time ($t = 0$) is negligible.

(iv) The effect of irradiation on oxide conductivity during oxide growth is negligible.

(v) The electrolyte (water) conductivity σ_0 at the initial time (before water ingress into the cladding gap) is constant ($3{\cdot}10^{-4}$ S/m). After water ingress, electrolyte conductivity σ is influenced by gamma and neutron fluxes through the phenomenon of radiolysis.

In the model shown in Figure 2, the water electrolyte occupies a distance d between two opposite electrodes. The Laplace equation in the electrolyte domain is given as

$$\nabla^2 \varphi = 0, \tag{1}$$

where φ is the electrostatic potential in the electrolyte. The current distribution is determined by

$$j = \sigma \nabla \varphi, \tag{2}$$

where j is the current density and σ is the electrolyte conductivity [7].

The mesh and boundary conditions used in the model are as shown in Figure 3. The three boundary conditions used in this model are enumerated as follows:

(i) Beyond the electrodes, the boundaries are considered insulating, which can be expressed by $\vec{n} \cdot \vec{j} = \vec{0}$, the so-called Neumann conditions [7], with $\vec{n}$ being the normal outward vector and $\vec{j}$ being the flux across the boundary.

(ii) At the cathode, the current density follows a Tafel-like law [7]:

$$i_c = -i_c^0 \exp\left(-\frac{V - V_{0c}}{b_c}\right), \tag{3}$$

where i_c^0 is the density of current exchange, b_c is the Tafel coefficient, V_{0c} is the potential of the O_2/H_2O couple, and V is the electrode potential. A constant i_c^0 supposes a constant concentration of dissolved oxygen in the electrolyte.

(iii) For the anodic oxidation of zirconium, an experimental polarization curve was obtained for Zry-2 at 295°C by Cox [7]. The result obtained by Cox is fitted with the following function:

$$i_a = i_a^0\left(1 - \exp\left(-\frac{V - V_{0a}}{b_a}\right)\right). \tag{4}$$

The parameters i_a^0, b_a, and V_{0a} are the density of current exchange at the anode, the anodic Tafel coefficient, and the potential of the O_2/H_2O couple, respectively, while V is the electrode potential.

(iv) The common potential of Zry-2 and the CEs was arbitrarily set to zero and thus does not appear explicitly in the equations.

(v) The minimum and maximum element size of the mesh in Figure 3 is chosen as $2.92{\cdot}10^{-5}$ and 1.456^{-2} mm, respectively.

2.2. Model Calibration. The present model is calibrated using data from the SC of Zircaloy cladding in a BWR [7], which agree with the results of the MIT experiments. In contrast to the reference model that is a plane geometry without crack or geometric imperfection, our model is a ¼ circular geometry with cracks as described above. Essentially, an oxide layer thickness of 19.98 μm is grown on the Zry-2 surface for corrosion lasting 1166 h with a 0.5 mm distance between the electrodes when the electrolyte conductivity was set to a constant value of $3{\cdot}10^{-4}$ S/m. The electrochemistry module of COMSOL Multiphysics 5.2 was used to compute the total electrode thickness change as well as the electrolyte current density. The difference in oxide thickness with respect to the reference standard (20 μm) is due to the nature of geometry. The electrode properties and other parameters used for this study are listed in Table 3.

2.3. Dose Rate Estimation on Cathode Surface. For all simulations in this work, it is assumed that the cathode surface is made up of a mixed field of neutron and gamma radiations during normal reactor operation, and the fast neutron flux on the electrode surface is $9.5{\cdot}10^{13}$ n/cm$^2{\cdot}$s [13]. The dose rate

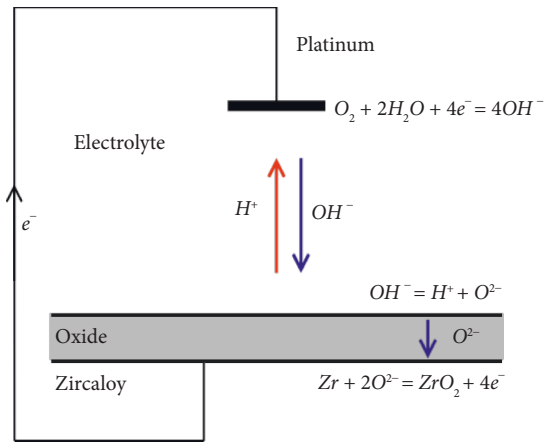

Figure 1: Lysell's electrochemical mechanism explaining shadow corrosion [7].

Table 1: Chemical composition of Alloy 718 [11].

Ni (%wt)	Cr (%wt)	Fe (%wt)	Nb + Mo + Ti (%wt)
53	19	19	9

Table 2: Chemical composition of Zry-2 [11].

Zr (%wt)	Sn (%wt)	Fe (% wt)	Cr (%wt)	Ni (%wt)
Bal.	1.32	0.169	0.108	0.055

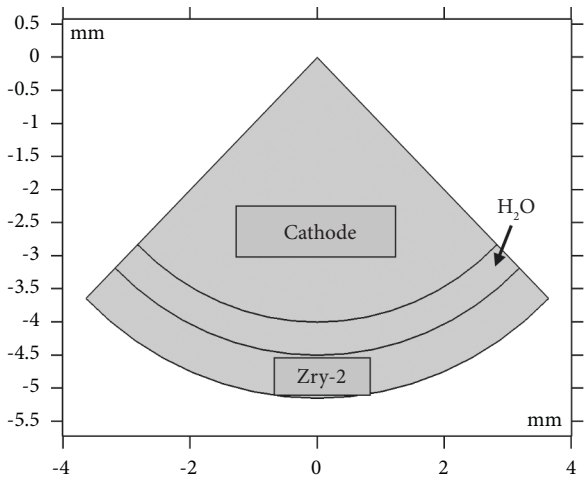

Figure 2: Model geometry used in this study.

$\dot{D}_n$ (Gy/s) due to neutrons at a particular point on the cathode surface is subsequently estimated. For neutrons with an average energy of 2 MeV, the neutron flux is converted to the dose rate using the conversion factor 1.5120E-01 (mrem/h)/(n/cm^2·s) [14] according to the following equation:

$$\dot{D}_{n(2\text{MeV})}\left[\frac{mrem}{h}\right] = 1.5120 \cdot 10^{-1}\left[\frac{mrem/h}{n/\text{cm}^2 \cdot s}\right] \cdot \text{Neutron flux}\left[n/\text{cm}^2 \cdot s\right], \quad (5)$$

where 1 $(mrem/h) = 2.7777\text{E}{-}09$ Gy/s.

To account for the gamma radiation field, a ^{137}Cs γ-source with a half-life of 30.1 years and an average gamma energy of 0.662 MeV is used in this study; hence, the conversion factor 1.52E-06 (rem/h)/(g/cm^2·s) is applied to convert γ flux into dose rate $\dot{D}_\gamma$ (Gy/s) as follows [14]:

$$\dot{D}_{\gamma(0.662\,\text{MeV})}\left[\frac{\text{rem}}{h}\right] = 1.52 \cdot 10^{-6}\left[\frac{\text{rem}/h}{g/\text{cm}^2 \cdot s}\right] \cdot \text{Gamma flux}\left[g/\text{cm}_2 \cdot s\right], \quad (6)$$

where gamma flux = 9.76·10^{14} g/cm^2·s at the point of interest on the cathode surface [15].

2.4. Estimation of H^+ and OH^- Concentrations. Under normal circumstances, the conductivity of water at room temperature is usually very low with a neutral pH of 7. This is due to low concentrations of hydrogen (H^+) and hydroxyl (OH^-) ions. However, the water chemistry condition used in the present study is the standard pH-11, which corresponds to the ionic product of water at 561 K and 10 MPa, which is equal to 10^{-11} $(\text{mol/l})^2$. The neutral pH in this condition (reactor) is 5.5, which implies that the H^+ and OH^-concentrations are both equal to 3.1623E-06 mol/l [7]. The density of water as a function of temperature at the prescribed physical conditions in this work is given as follows [16]:

$$\rho_{H_2O} = 112.07T^{-1.286}, \quad 560 \le T \le 1273, \quad (7)$$

where ρ_{H_2O} and T have units of $g\cdot\text{cm}^{-3}$ and K, respectively. The data that generated equation (7) has an accuracy of 0.9873.

When water or dilute aqueous solutions are irradiated, electrons, hydrogen, and hydroxyl radicals are produced. In the radiation energy treatment of water, the number of free radicals created by radiation and how it varies with pH and dissolved oxygen are essential issues [17]. As a result of irradiation, water undergoes radiolysis in the cladding gap, thereby producing hydroxyl radicals. The G-value (mol/100 eV) due to neutron and gamma irradiations is expressed by equations (8) and (9), respectively [18],

$$G_n = 0.99 + 0.00626q, \quad (8)$$

$$G_\gamma = 2.557 + 0.01012q, \quad (9)$$

where q is the temperature in °C. With known dose rates and G-values for each of the considered radiations, the production rate of OH^- is evaluated as follows [19]:

$$S_r = \sum_{r=1}^{2} \frac{\dot{D}_r \cdot G_{r\text{OH}^-} \cdot \rho_{\text{H}_2\text{O}}}{1.602 \cdot 10^{-19} \cdot N_A}, \quad (10)$$

where $r = 1, 2$ represents neutrons and gamma, respectively, $\dot{D}_r$ is the dose rate for a given radiation type r (Gy/s), $G_{\text{rOH}-}$ is the radiolytic yield for a given radiation type r (molecules/100 eV), $\rho_{\text{H}_2\text{O}}$ is water density (g/cm^3), and N_A is Avogadro's number. The product

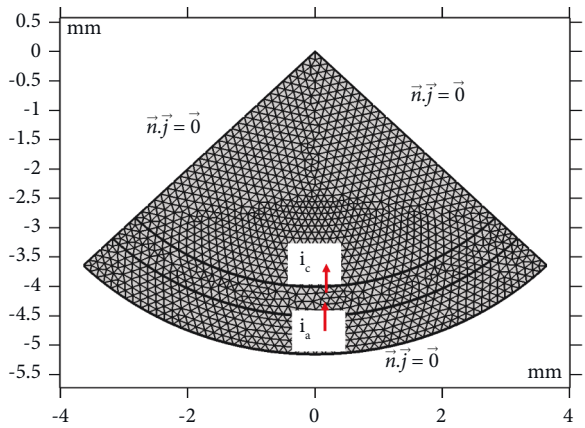

Figure 3: Mesh and boundary conditions used in computations. Beyond the electrodes, the boundaries are insulating.

$$S_r t = C_{OH^-}, \tag{11}$$

is a measure of the concentration (mol/dm^3) of OH^- ions in the cladding gap at time t. At the standard operating time ($t = 1166$ h), the pOH of the electrolyte can be evaluated using the result of equation (11),

$$\text{pOH} = -\log_{10} C_{OH^-}. \tag{12}$$

In turn, equation (12) is used to compute the pH and then the concentration of H^+ in the electrolyte, knowing that at the prescribed condition,

$$\text{pH} = 11 - \text{pOH}. \tag{13}$$

2.5. Computation of the Molar Conductivity of the Electrolyte. The quantity of ions in a given volume of a solution determines its conductivity. Electrolytes are ionic conductors (charge carriers are ions) unlike metals that are electronic conductors (charge carriers are electrons). It has been noted that the conductivities of hydrogen and hydroxyl ions are unexpectedly high, being about 7 and 3 times that of the average value for other ions, respectively [20]. Accordingly, it is assumed that, apart from these two ions (H^+ and OH^-), the contribution of other ions to the electrolyte conductivity is negligible. The Nernst–Einstein equation, which links molar conductivity to diffusion coefficients, can be written as follows [21]:

$$\Lambda = \left(\frac{\sigma}{c}\right) = \left(\frac{F^2}{RT}\right)\alpha\left(D^+ + D^-\right), \tag{14}$$

where σ is the intrinsic conductivity, c is the molar concentration, F is the Faraday number, R is the gas constant, T is the absolute temperature, α is the degree of dissociation of the electrolyte, and D^+ and D^- represent the variable diffusion coefficients (m^2/s) of H^+ and OH^-, respectively. When the molar conductivity Λ takes a zero value, ions cannot diffuse, i.e., $\alpha = 0$ and $\alpha = 1$ imply that the degree of dissociation is highest (complete dissociation). In this work, Λ is computed by discretization of the degree of dissociation α, between 0 and 1. The temperature-dependent diffusion coefficients ($D^{\pm}$) of the ions (H^+ and OH^-) are linearized in the coordinates of the Arrhenius equation [22] according to the following equation:

$$D^{\pm} = D_0^{\pm} \cdot \exp\left(-\frac{E_a}{RT}\right), \tag{15}$$

where $D_0^{\pm}$ is temperature independent, R is the gas constant (8.3145 J/mol/K), T is the absolute temperature, and E_a is the diffusion activation energy. The values of $D_0^{\pm}$ and E_a for H^+ and OH^- are obtained from the open literature [23]. In this work, the value of electrolyte conductivity $\sigma_0 = 3{\cdot}10^{-4}$ S/m was adopted as the initial condition, while at a stipulated time ($t = 1166$ h), the following equation was used to compute the electrolyte conductivity:

$$\sigma = \sigma_0 + \sigma_t, \tag{16}$$

where

$$\sigma_t = \left(\Lambda_{H^+} \cdot C_{H^+}\right) + \left(\Lambda_{OH^-} \cdot C_{OH^-}\right), \tag{17}$$

is the contribution of H^+ and OH^- ions to the electrolyte conductivity at a given time t. With the aid of the electrochemistry module of COMSOL Multiphysics 5.2, the current and potential distributions in the electrolyte sandwiched between two opposing electrodes are computed using an electrostatic model adapted for the study of shadow corrosion.

3. Results and Discussion

3.1. Effect of Irradiation on Electrolyte Conductivity. At typical BWR working conditions (temperature of 561 K and pressure of 10 MPa), the dose rates computed at a given location on the cathode surface using equations (5) and (6) are 39,900 and 4,108 Gy/s for neutrons and gamma, respectively. With this information, the electrolyte conductivity is evaluated by measuring the production rate of OH^- and H^+ ions in the cladding gap. As expressed by equation (14), Figure 4 depicts the electrolyte conductivity, Λ, as a function of the degree of dissociation of water, α.

As evident from Figure 4, conductivity increases proportionally to the degree of dissociation α. A zero-degree dissociation (i.e., $\alpha = 0$) corresponds to the initial conditions where the electrolyte conductivity is $3{\cdot}10^{-4}$ S/m. As water undergoes radiolysis in the cladding gap due to the action of ionizing radiations, water molecules are split into constituent ions and the degree of dissociation begins to rise. At complete dissociation (i.e., $\alpha = 1$), the highest electrolyte conductivity is recorded as $10.375{\cdot}10^{-4}$ S/m.

3.2. Estimation of Oxide Growth for Plane and Circular Geometries. To validate the model used in the current work, the parameters used for the plane geometry in ref [7] were first applied to develop a similar model. Then, the model is adapted to develop a new model for the 1/4 circular geometry presented in this work. Figure 5 shows the

Table 3: Model parameters used in the simulation.

Variables	Values used for calibration [7]	Present work	
		Case 1 (circular geometry with a platinum cathode)	Case 2 (circular geometry with an alloy 718 cathode)
$V_{0c}/SHE(V)$	−0.21	−0.21	−0.20 [11]
$b_c\,(mV)$	120	120	180 [12]
$i_c^0\,(\mu Acm^{-2})$	0.8	0.8	0.4 Ref [11]
$V_{0a}/SHE(V)$	−0.9	−0.9	−0.9
$i_a^0\,(\mu Acm^{-2})$	10	10	10
$b_a\,(V)$	0.1	0.1	0.1
T (K)	561	561	561
$\sigma_0\ (\mathrm{Sm}^{-1})$	$3{\cdot}10^{-4}$	$\sigma = \sigma_0 + \sigma_t$	$\sigma = \sigma_0 + \sigma_t$
d (mm)	0.5	0.05–5	0.05–5

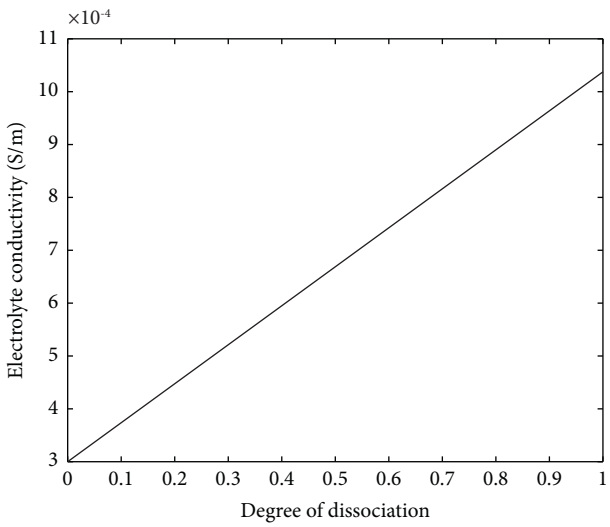

Figure 4: Electrolyte conductivity versus degree of dissociation of water in the cladding gap.

electrostatic potential in the electrolyte around a platinum cathode at a cladding separation of 0.5 mm. It can be seen that the shadow of the counter-electrode is imprinted on the anode with the implication of oxide growth in the opposite direction. The arrow lines in this figure represent the current density vector whose magnitude is the electric current per unit area at a given point, its direction being that of the motion of positive ions at this point. Contrary to a uniform radial electrostatic distribution in an uncracked geometry (Figure 5(b)), it is observed that the radial electrostatic potential distribution has a peak character in a cracked geometry with a value of 1.17 V at the tip of the cracks (Figure 5(a)). This is attributed to the tendency of charges/ions to concentrate at sharp points.

The oxide growth due to SC was computed as the total electrode thickness changes, which occurred for the prescribed time period ($t = 1166$ h). Figure 6(a) shows the result for a plane geometry adapted from ref [7], while Figure 6(b) is the result for this work in a 1/4 circular geometry, both obtained under the same working conditions. In the former case, shadow corrosion produced a bell-shaped oxide layer that is localized with a peak value of 20 μm cast opposite the center of the Zry-2 cladding. Since the cathode and anode have respective lengths of 2 and 16 mm (equivalent to a cathode/anode ratio of 0.125), it is obvious that the cathode is localized in the SC field. Therefore, the localized bell-shaped oxide profile observed in this case is largely due to a localized cathode. In the latter scenario, the shadow corrosion is not localized but uniform across the smooth internal surface of Zry-2 cladding with an oxide layer value of 20 μm. This is expected because the cathode/anode ratio is ≈1; hence, we have a distributed source giving rise to a uniform oxide profile. It is further observed in this case that the oxide growth is irregular around the vertices of the anode, giving rise to a zig-zag oxide pattern that terminates in a maximum peak. This observation is a result of an overlap of the oxide growth at the vertices (Figure 7). The maximum oxide peak due to the overlap at the anode vertices is 32.1 μm, whereas a uniform oxide layer of 20 μm is spread across the smooth internal surface of Zry-2.

3.3. Dynamics of Shadow Corrosion under Varying Electrode Separation and Electrolyte Conductivities. Among the factors affecting SC are the separation between electrodes and electrolyte conductivity. These two factors were investigated by measuring the oxide thickness as a function of electrode separation while keeping electrolyte conductivity constant. Figure 8 shows the result obtained when platinum was used as the CE. Compared to the experimental result reported for a plane geometry in [7], the present work reveals that at 0% electrolyte dissociation (corresponding to an electrolyte conductivity of $3{\cdot}10^{-4}$ S/m), shadow corrosion in a circular geometry has an exponential characteristic similar to the one obtained in a plane geometry. The values used for this comparison are the maximum oxide layer peaks reported in a plane geometry and the uniform oxide layer cast on the smooth surface of Zry-2 at locations other than the vertices. It is evident from Figure 8(a) that between 0 and 20% dissociation of the electrolyte, the general exponential trend of SC is conserved within electrode separation of 0.5–5 mm. At higher degrees of dissociation ($\alpha \geq 0.5$), however, the oxide growth is constant between the 0.5 and 1.5 mm electrode gap, and the graph begins to assume a fairly linear shape after a 2 mm gap (Figure 8(b)). This suggests that the electrolyte (water) is perhaps never completely ionized in the gap under the reactor working conditions. It is also observed

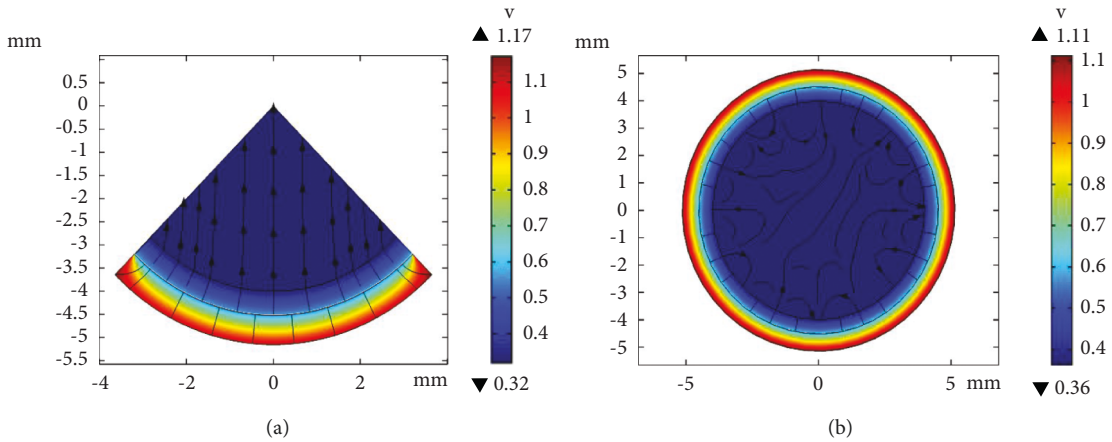

Figure 5: Electrostatic potential distribution in the electrolyte near the counter-electrode in a (a) ¼ circular geometry and (b) circular geometry.

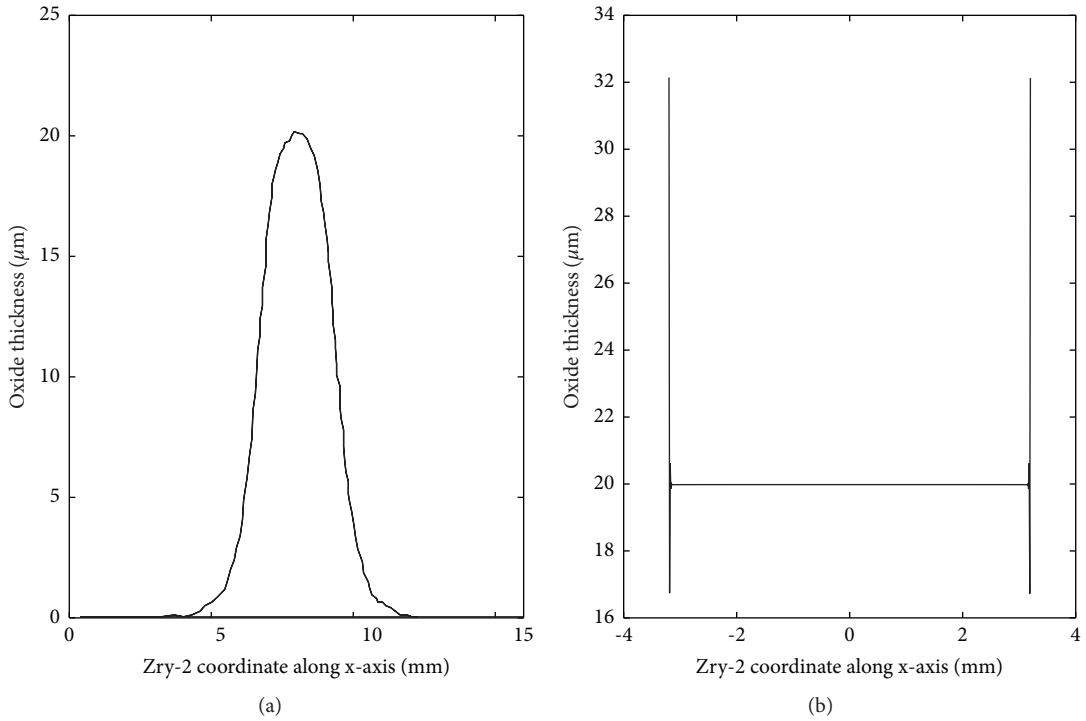

Figure 6: Comparison of oxide thickness profiles obtained under the same working conditions with platinum as CE (a) for Zry-2 in a plane geometry [7] and (b) for Zry-2 in a ¼ circular geometry.

from both graphs that irrespective of the degree of dissociation, the same oxide thickness is obtained at a cladding gap of 0.5 mm for both plane and circular geometries. This observation is in conformity with the experimental result of [24] that reported the same oxide thickness for corrosion occurring at a constant electrode separation whatever the nature of the CE, provided it is made of a metal nobler than the Zircaloy. The role of the counter-electrode is then essentially that of a cathode and that shadow corrosion is dominated by a mechanism of electrochemical character. Furthermore, the result obtained in this work is in agreement with the results from the test in the R2 reactor in Studsvik [24] where radiolysis was identified to have an important role for the formation of shadow corrosion.

Statistical data of the maximum oxide layer at selected cladding gaps are presented in Tables 4 and 5. Table 4 shows that at cladding gap $d \leq 0.5$ mm, the zirconia layer on the smooth internal surface of Zry-2 is a constant value, ~20 μm, irrespective of the degree of dissociation. Above 0.5 mm electrode separation, the oxide layer begins to drop as a function of d at constant α, while the oxide layer grows as α rises at cladding separation beyond 0.5 mm. The situation is

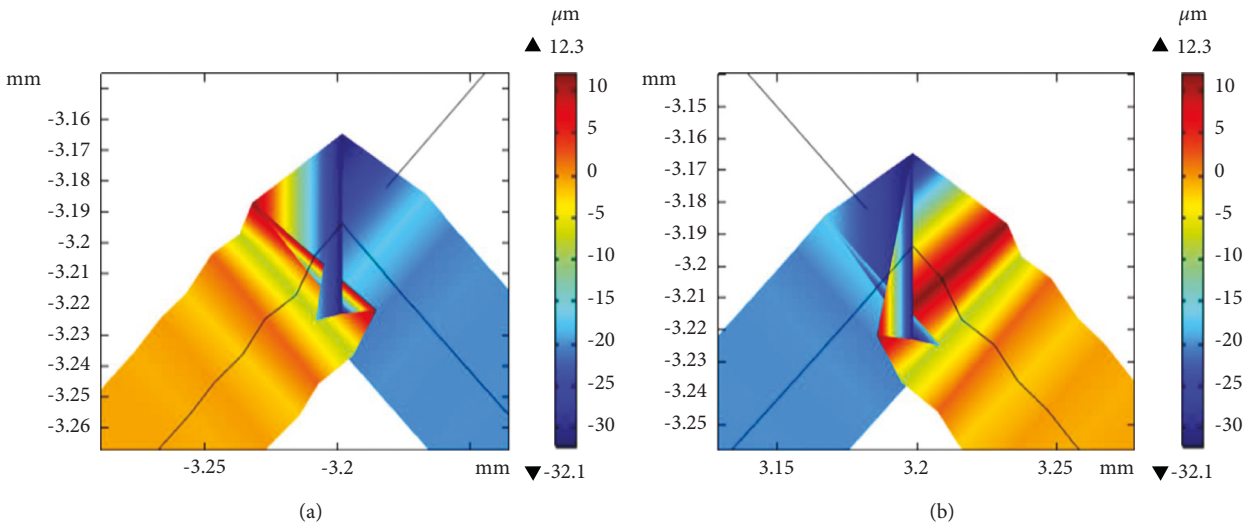

FIGURE 7: Overlap of oxide growth at the vertices of Zry-2 (a) left vertex and (b) right vertex. Away from the vertices, oxide growth is uniform (blue field). The negative values on the legend indicate the presence of shadow corrosion, and the oxide thickness is obtained by multiplying the values on the legend by −1.

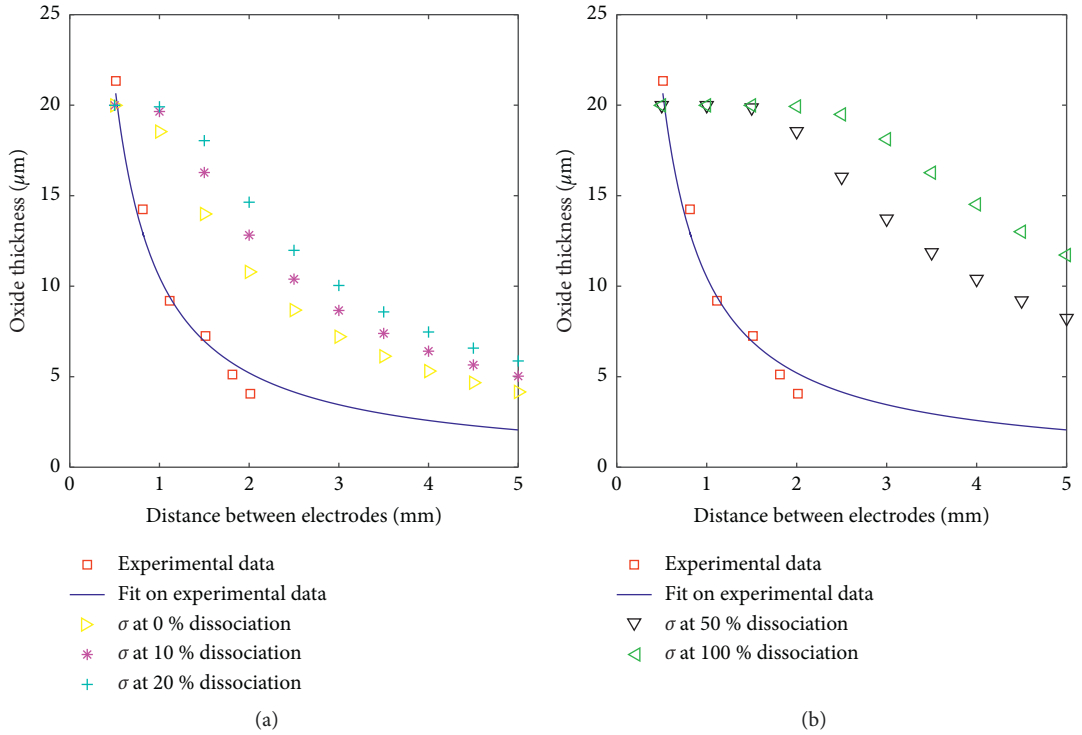

FIGURE 8: Maximum oxide thickness for several distances between electrodes at (a) 0, 10, and 20 and (b) 50 and 100% degrees of dissociation.

similar around the vertices of the anode (Table 5) where oxide growth due to overlap is fairly constant at $d \leq 0.5$ mm. At a cladding gap of above 0.5 mm, oxide growth at vertices due to overlap is proportional to the degree of dissociation of the electrolyte. This shows that the anode vertices are more sensitive to shadow corrosion than the smooth surface. Furthermore, it is observed that the size of elements that make up the mesh influences the oxide characteristics at the vertices; the smaller the size, the higher the overlap.

3.4. Comparison of Shadow Corrosion under Different Cathodes. This section discusses the parameters i_c^0 (density of current exchange at the cathode) and b_c (cathodic Tafel coefficient) and how they affect the cathodic current, as shown in equation (3). This experiment was done by running two parallel simulations with two different cathodes while keeping the anode constant. In the first case, the cathode was chosen as platinum, while in the second case, nickel was used. Figures 9 and 10 show the SC results for platinum and nickel counter-electrodes, respectively. Figures 9 and 10

Table 4: Variation of oxide thickness as a function of the degree of dissociation (α) for an arbitrary smooth surface of Zry-2.

α	Oxide thickness (μm) at various electrode distances d				
	$d = 0.08$ mm	$d = 0.5$ mm	$d = 1.0$ mm	$d = 2.0$ mm	$d = 5.0$ mm
0	19.99	19.98	18.54	10.79	4.16
0.1	19.99	19.99	19.65	12.81	5.03
0.2	19.99	19.99	19.90	14.64	5.87
0.5	19.99	19.99	19.99	18.55	8.23
1	19.99	19.99	19.99	19.93	11.72

Table 5: Variation of oxide thickness as a function of the degree of dissociation (α) at Zry-2 vertices.

α	Oxide thickness (μm) at various electrode distances d				
	$d = 0.08$ mm	$d = 0.5$ mm	$d = 1.0$ mm	$d = 2.0$ mm	$d = 5.0$ mm
0	31.9	32.1	27.6	12.5	4.16
0.1	31.9	32.1	30.8	15.8	5.03
0.2	31.9	32.2	31.7	19.2	6.01
0.5	32.0	32.1	31.9	27.9	9.06
1	32.0	32.1	32.1	31.8	14.4

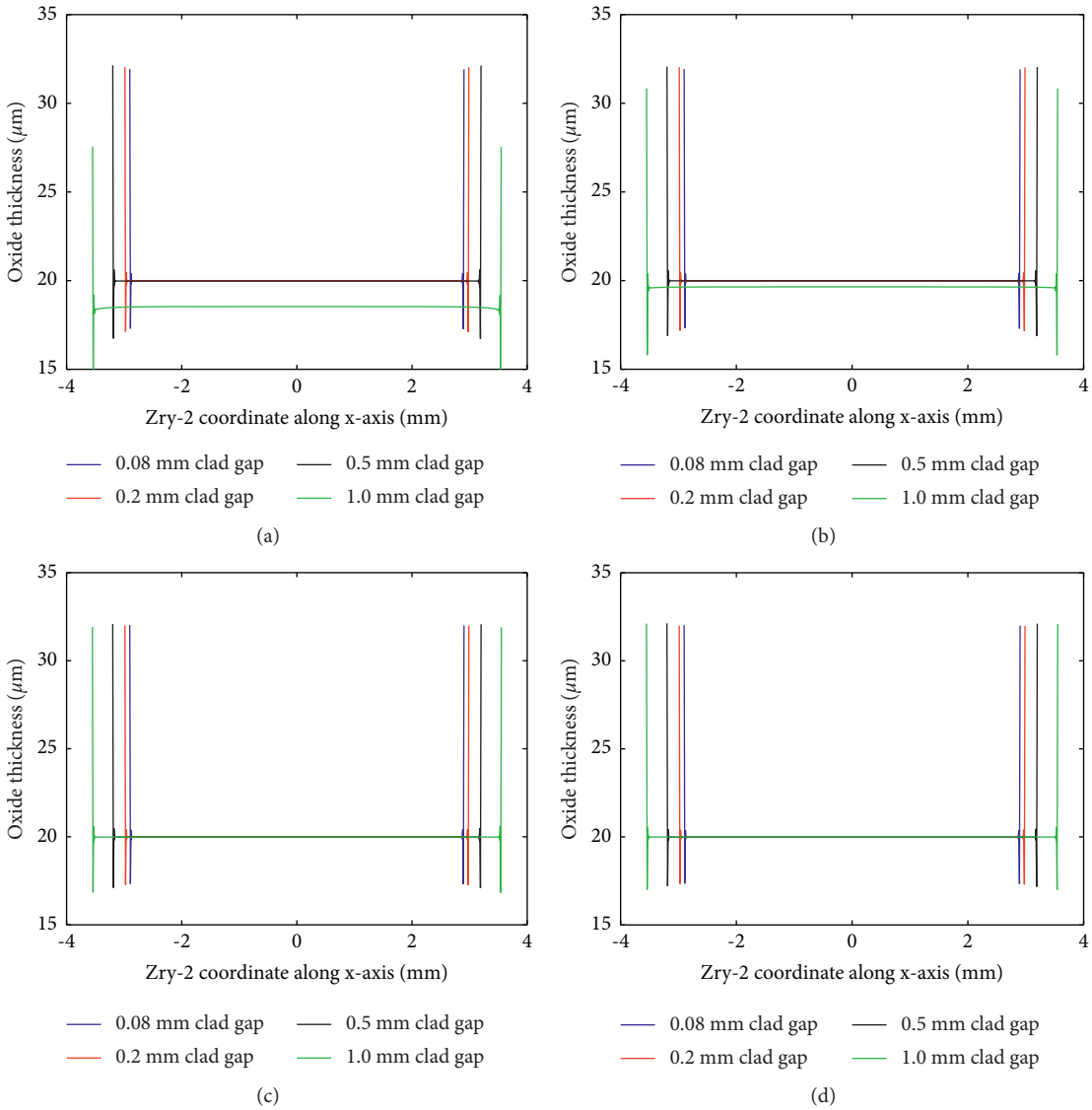

Figure 9: SC results for platinum CE with electrolyte conductivities: (a) 3.0E-4 S/m, (b) 3.7E-4 S/m, (c) 6.7E-4 S/m, and (d) 10.4E-4 S/m.

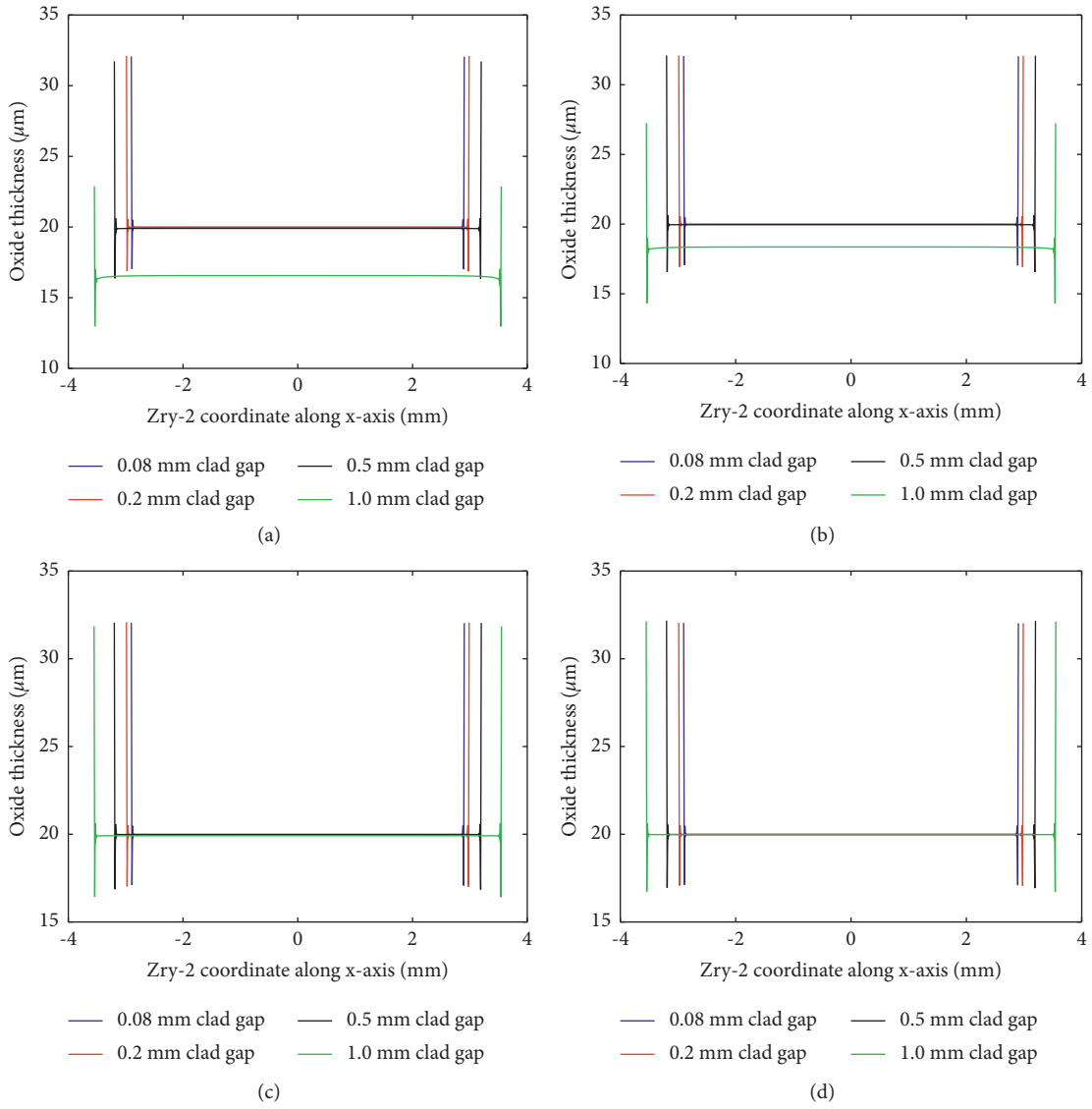

Figure 10: SC results for nickel CE with electrolyte conductivities: (a) 3.0E-4 S/m, (b) 3.7E-4 S/m, (c) 6.7E-4 S/m, and (d) 10.4E-4 S/m.

were obtained at electrolyte conductivities of 3E-4, 3.7E-4, 6.7E-4, and 10.4E-4 S/m, corresponding to 0, 0.1, 0.5, and 1 degrees of dissociation.

From Figures 9 and 10, it is seen that regardless of the cathode nature, the oxidation profiles are similar. Again, this buttresses our earlier position that whatever the type of the CE (provided it is made of a metal nobler than the Zircaloy), the resulting oxide profiles are the same. From equation (3), it suffices to say therefore that the parameter that determines the oxide growth is predominantly the potential of the O_2/H_2O couple (V_{0C}) and not the density of current exchange at the cathode (i_c^0), neither is it the cathodic Tafel slope (b_c). In other to justify this finding, a third parallel simulation was performed by keeping V_{0c} constant while increasing i_c^0 and b_c by a factor of 5 and 3, respectively, for the standard case. The resulting values of i_c^0 ($4\,\mu A\,cm^{-2}$) and b_c (370 mV) in this parametric study correspond to the electrochemical characteristics of UO_2 as a cathode as obtained in [25]. The resulting oxide profiles for such a parametric study were practically the same on the smooth internal surface of Zry-2 like those shown in Figure 9. For both electrode types investigated, the oxide layer is 20 μm for electrode spacing of 0.08, 0.2, and 0.5 mm irrespective of the electrolyte conductivity. When the spacing between electrodes reaches 1 mm and beyond, the oxidation profile becomes largely dependent on the electrolyte conductivity. This result confirms that SC has a limiting minimum electrode separation below which the oxide growth remains constant, and for this work, the limiting value is 0.5 mm. At an electrolyte conductivity of $3{\cdot}10^{-4}$ S/m, the oxide layer on the smooth surface of Zry-2 is 18.54 μm at an electrode spacing of 1 mm, while the oxide peak at the vertices is 27.6 μm for the platinum cathode. For the nickel cathode, the values obtained at similar conditions are 16.56 and 22.9 μm. The difference in oxide profiles for both cathodes is due to the dissimilar potential of the O_2/H_2O couple (V_{0c}).

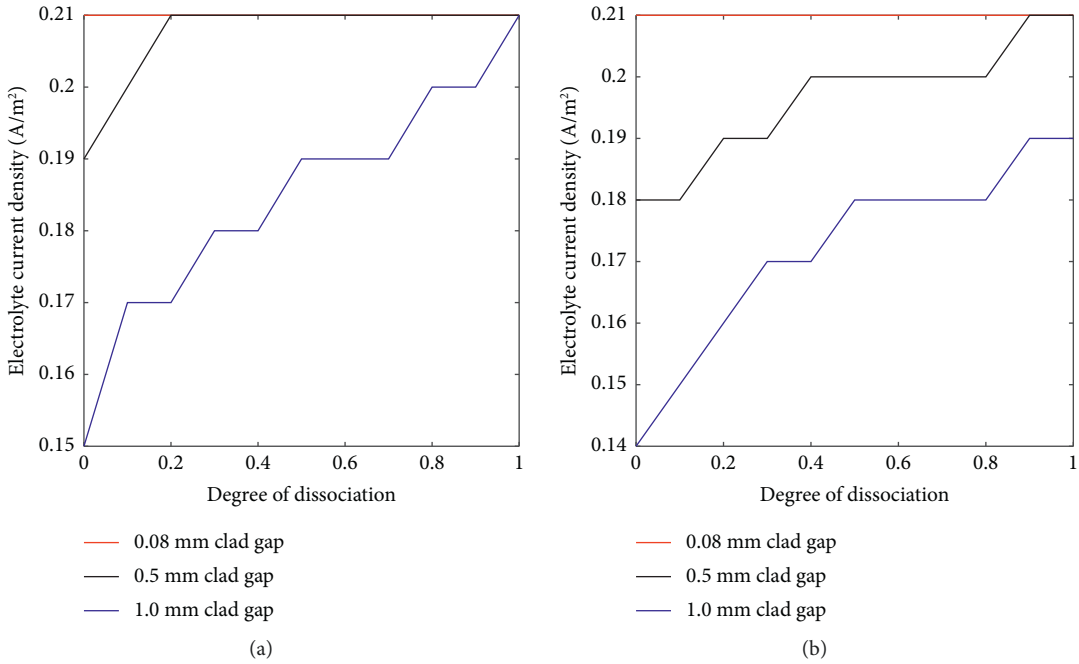

Figure 11: Electrolyte current densities as a function of the degree of dissociation for (a) platinum and (b) nickel counter-electrodes.

3.5. Corrosion Rate Prediction. The rate of corrosion, C_R, occurring at the cladding gap can be calculated from current density using Faraday's law [26] as follows:

$$C_R = \frac{M}{zF\rho} j_x, \tag{18}$$

where the Faraday constant F is 96485.34 C·mol^{-1}, the atomic mass M is 123 and 91.224 g·mol^{-1} for ZrO_2 and Zry-2, respectively [7], the density ρ is 5840 and 6510 kg·m^{-3}, respectively, for ZrO_2 and Zry-2 [7, 27] for the corroding constituents, the electron number z is 4, the corrosion rate C_R is in ms^{-1}, and the current density j_x is in Am^{-2}. Figure 11 shows the current densities recorded at the cladding gap for the two scenarios investigated.

Figures 11(a) and 11(b) show that the current density is constant at a cladding gap of 0.08 mm for platinum and nickel counter-electrodes. The value recorded is 0.21 A/m^2, and since this occurs at the typical cladding gap of a fuel pellet, it implies that the corrosion rate is constant at the gap irrespective of the degree of dissociation or electrolyte conductivity. At higher cladding gaps, the corrosion rate differs for both CEs. The difference could be attributed to the cathodic exchange current density i_c^0 and cathodic Tafel coefficient b_c that are different for both counter-electrodes.

Using equation (18), the corrosion rate of Zry-2 at a cladding gap of 0.08 mm is $2.405{\cdot}10^{-1}$ mm·py (mm per year) for both counter-electrodes. The C_R value obtained in this work is high compared to the result of [28] that recorded a corrosion rate of $1.693{\cdot}10^{-3}$ mm·py. The difference is due to the water chemistry condition in the latter work (temperature = 298 K, pH = 6.8, and current density = $1.473{\cdot}10^{-3}$ A/m^2), which is different from those in this work (temperature = 561 K, pH = 5.5, and current density = $2.1{\cdot}10^{-1}$ A/m^2). When electrode separation ≥0.5 mm, C_R becomes largely dependent on the degree of dissociation of the electrolyte. In the case of a platinum cathode (Figure 11(a), at an electrode spacing of 0.5 mm), C_R rises initially from $2.1759{\cdot}10^{-1}$ mm·py at 0% electrolyte dissociation and attains a stable value of $2.405{\cdot}10^{-1}$ mm·py at 20% electrolyte dissociation. At $d = 1$ mm, the growth in C_R becomes more sluggish, starting at $1.7178{\cdot}10^{-1}$ mm·py for 0% electrolyte dissociation and terminating at $2.1759{\cdot}10^{-1}$ mm·py for 100% electrolyte dissociation using platinum as CE. The situation is similar for the nickel CE investigated (Figure 11(b)). However, the electrolyte current density (which determines the corrosion rate) exhibits an intermittent plateau character in the course of radiolysis. This was observed at a 0.5 mm electrode spacing for nickel CE and at a 1 mm electrode spacing for both CEs. This observation suggests that the accumulation of hydrogen (H^+) and hydroxyl (OH^-) ions during radiolysis has a latent character.

4. Conclusion

This work shows that shadow corrosion in a ¼ circular geometry has similarities and differences with those observed in a plane geometry. Like SC observed in a plane geometry, the anodic oxide growth in this work obeys an exponential law at lower degrees of dissociation ($\alpha \leq 0.2$) when the separation between electrodes is 0.5–5.0 mm. Whereas SC is localized in a plane geometry, the situation is different in a ¼ circular geometry where SC is uniform on the smooth surface of the anode with maximum peaks at the vertices of the anode. It has also been established that below 0.5 mm electrode separation, the oxide thickness on a smooth surface has a constant value of 20 μm irrespective of the electrolyte conductivity. A similar trend was observed at the anode vertices where the oxide grows inversely to d,

provided $d > 0.5$ mm. The above observations are the same irrespective of the type of counter-electrode used. This work has also revealed that on the surface of the UO_2 fuel pellet where neutrons and gamma doses reach respective values of 39.9 and 4.1 kGy/s, the corrosion current density could reach $2.1 \cdot 10^{-1}$ A/m^2 in a cladding gap of 0.08 mm. This results in a high corrosion rate of $2.405 \cdot 10^{-1}$ mm·py for Zry-2, a value that is 142 times greater than that obtained at room temperature in the absence of irradiation. The corrosion rate falls at higher cladding gaps depending on the degree of dissociation of the electrolyte.

The current work improves the understanding of the similarities and differences between the shadow corrosion in one-fourth circular and plane geometries. However, as a limitation, further work is needed to reduce the model assumptions made in this work, towards real-world applications. Nevertheless, this work serves as a useful foundation for advanced research on fuel pellet optimization and the protection of fuel cladding integrity.

Data Availability

No data are available on request.

Conflicts of Interest

The authors declare that they have no conflicts of interest.

Acknowledgments

The authors are grateful to the China Scholarship Council (CSC) for the scholarship grant that has greatly facilitated this research. Qingyu Wang acknowledges the support from the Fundamental Research Funds for the Central Universities (3072021CF1501) of Harbin Engineering University. This study was funded by the Fundamental Research Funds for the Central Universities (3072021CF1501) of Harbin Engineering University.

References

[1] M. Howlader, C. Kinoshita, K. Shiiyama, M. Kutsuwada, and M. Inagaki, "In situ measurement of electrical conductivity of Zircaloy oxides and their formation mechanism under electron irradiation," *Journal of Nuclear Materials*, vol. 265, no. 1-2, pp. 100–107, 1999.

[2] M. M. R. Howlader, K. Shiiyama, C. Kinoshita, M. Kutsuwada, and M. Inagaki, "The electrical conductivity of zircaloy oxide films," *Journal of Nuclear Materials*, vol. 253, no. 1-3, pp. 149–155, 1998.

[3] B. Cox, "Rate controlling processes during the pre-transition oxidation of zirconium alloys," *Journal of Nuclear Materials*, vol. 31, no. 1, pp. 48–66, 1969.

[4] P. J. Shirvington, "A mechanism for in-reactor oxidation of zirconium alloys from oxide electrical characteristics: (I). Zircaloy-2," *Journal of Nuclear Materials*, vol. 50, no. 2, pp. 183–199, 1974.

[5] N. Ramasubramanian, "Shadow corrosion," *Journal of Nuclear Materials*, vol. 328, no. 2-3, 2004.

[6] F. Garzarolli, P. B. Hoffmann, and A. Seibold, "Shadow corrosion or crevive corrosion?" *Journal of Nuclear Materials*, vol. 289, no. 3, pp. 338–341, 2001, 289.

[7] P. Buttin, B. Malki, P. Barberis, and B. Baroux, "Numerical analysis of the galvanic coupling in the shadow corrosion of zirconium alloy," *Journal of Nuclear Materials*, vol. 420, no. 1-3, pp. 591–596, 2012.

[8] IAEA-Tecdoc-996, *Waterside corrosion of zirconium alloys in nuclear power plants*, IAEA, Vienna, Austria, 1998.

[9] T. Shikama and G. Pells, "A comparison of the effects of neutron and other irradiation sources on the dynamic property changes of ceramic insulators," *Journal of Nuclear Materials*, vol. 212-215, pp. 80–89, 1994.

[10] P. Wang, K. Nowotka, and G. S. Was, "Reproducing shadow corrosion on Zircaloy-2 using in-situ proton irradiation," *Journal of Nuclear Materials*, vol. 558, Article ID 153406, 2022.

[11] P. Barberis, M. Skocic, D. Kaczorowski, D. Perche, Y. Wouters, and K. Nowotka, "Shadow corrosion: experiments and modeling," *Journal of Nuclear Materials*, vol. 523, pp. 310–319, 2019.

[12] P. K. R. Kuppam, K. M. M. D. K. Kimbulapitiya, S. Vuppala et al., "A nickel coated copper substrate as a hydrogen evolution catalyst," *Catalysts*, vol. 12, no. 1, 2022.

[13] R. L. Williamson, J. Hales, S. Novascone et al., "Multidimensional multiphysics simulation of nuclear fuel behavior," *Journal of Nuclear Materials*, vol. 423, no. 1-3, pp. 149–163, 2012.

[14] S.-G. L. Kwon, S. Y. Lee, and C.-C. Yook, *Calculation of Neutron and Gamma-Ray Flux-to-Dose-Rate Conversion Factors*, IAEA, Vienna, Austria, 1981.

[15] M. Brovchenko, B. Dechenaux, K. W. Burn, P. Console Camprini, I. Duhamel, and A. Peron, "Neutron-gamma flux and dose calculations in a pressurized water reactor (PWR)," *EPJ Web of Conferences*, vol. 153, 2017.

[16] W. Wagner and A. Pruß, "The IAPWS formulation 1995 for the thermodynamic properties of ordinary water substance for general and scientific use," *Journal of Physical and Chemical Reference Data*, vol. 31, no. 2, pp. 387–535, 2002.

[17] J. Goodisman and R. Blades, "Conductivity of irradiated pure water," *Journal of Physical Chemistry A*, vol. 104, 2000.

[18] A. E. o. C. Limited, "The reaction set, rate constants and g-values for the simulation of the radiolysis of light water over the range 20 to 350°C based on information available in 2008," *Nuclear Platform Research and Development*, 2009.

[19] N. L. Hansson, C. Ekberg, and K. Spahiu, "Alpha dose rate calculations for UO2 based materials using stopping power models," *Nuclear Materials and Energy*, vol. 22, Article ID 100734, 2020.

[20] G. N. Khang and C. L. Sai, "The concept of conductivity and molar conductivity of an aqueous solution," *Singapore Journal of Education*, vol. 3, no. 1, pp. 27–31, 1980.

[21] L. Garrido, A. Mejia, N. Garcia, P. Tiemblo, and J. Guzman, "Ion diffusion coefficients model and molar conductivities of ionic salts in aprotic solvents," *The Journal of Physical Chemistry B*, vol. 119, no. 7, pp. 3097–3103, 2015.

[22] V. I. Volkov, A. V Chernyak, D. V. Golubenko et al., "Hydration and diffusion of H(+), Li(+), Na(+), Cs(+) Ions in Cation-Exchange Membranes Based on Polyethylene- and Sulfonated-Grafted Polystyrene Studied by NMR Technique and Ionic Conductivity Measurements," *Membranes (Basel)*, vol. 10, 2020.

[23] S. H. Lee and J. C. Rasaiah, "Proton transfer and the mobilities of the H+ and OH- ions from studies of a dissociating model

for water," *The Journal of Chemical Physics*, vol. 135, no. 12, Article ID 124505, 2011.

[24] B. Andersson, *Test Reactor Studies of the Shadow Corrosion Phenomenon*, ASTM International, Pennsylvania, USA, 2002.

[25] C. G. Alecu, *Studies of Electrochemical Corrosion Processes OF UO2 and Mixed Oxide Fuels in Aqueous Solutions in the View of Final Storage of Spent Nuclear Fuel*, JRC Technical Notes, Karlsruhe, Germany, 2008.

[26] K. B. Deshpande, "Validated numerical modelling of galvanic corrosion for couples: magnesium alloy (AE44)–mild steel and AE44–aluminium alloy (AA6063) in brine solution," *Corrosion Science*, vol. 52, no. 10, pp. 3514–3522, 2010.

[27] IAEA, *Thermophysical Properties Database of Materials for Light Water Reactors and Heavy Water Reactors*, IAEA, Vienna, Austria, 2006.

[28] A.-A. F. Waheed, A.-H. T. Kandil, and H. M. Hamed, "Electrochemical corrosion of Zircaloy-2 under PWR water chemistry but at room temperature," *Annals of Nuclear Energy*, vol. 94, pp. 168–174, 2016.